Physics and Chemistry of Minerals (2021) 48:20
https://doi.org/10.1007/s00269-021-01145-7

ORIGINAL PAPER

Environmental-sulfur-controlled surface properties of pyrite: a first principles PBE + *U* study

Haiyang Xian[1,2] · Xiao Wu[1,2,3] · Jianxi Zhu[1,2] · Runxiang Du[1,2,3] · Jingming Wei[1,2,3] · Runliang Zhu[1,2] · Hongping He[1,2,3]

Received: 21 October 2020 / Accepted: 31 March 2021 / Published online: 19 April 2021

Abstract

The structure and stability of pyrite (100), (210), (110), and (111) surfaces in different sulfur conditions were studied in the framework of GGA(PBE) + *U* implementations of density functional calculations. The Hubbard *U* correction was found to be a critical parameter in density functional theory (DFT) calculations to describe pyrite surfaces. With the *U* correction, the surface energy order for stoichiometric pyrite surfaces is (100) < (210) < (110) < (111), which is different with previous knowledge from conventional DFT and classical force field calculations, but consistent with broken bonds number and shape distribution in natural and synthetic systems in different sulfur conditions. Within the considered surfaces, the stoichiometric (100)-S and non-stoichiometric (111)-3S are the most stable under both S-lean and S-rich conditions, respectively. For relative stable surfaces in different environment, (100)-Fe and (100)-2S reconstruct, but (111)-Fe and (111)-3S show no relaxations while (100)-S, (210)-Fe′, and (210)-2S′ show relaxations to certain degree. Electron transfer from surface Fe to S atom on pyrite during relaxation and reconstruction, forming exemplary surface configuration and chemical composition. These findings reveal the nature of pyrite surfaces in various sulfur conditions, proving fundamental not only for surface-related applications but also for geological indicators of pyrite formation conditions.

Keywords Pyrite · Surface science · Surface energy · Surface stability · DFT + *U* · Hubbard *U*

Introduction

The surface nature of pyrite has received wide interests, attributed by its multidisciplinary importance in environmental, geochemical, and photochemical processes (Murphy and Strongin 2009). The reactivity between organic xanthates (Chen et al. 2013; Deng et al. 2013; Zhang et al. 2013), metal ions (Yang et al. 2016) and pyrite surface plays a main role in floatation of pyrite. The oxidation, dissolution, and adsorption/reduction of pyrite surface are responsible for acid mine drainage (AMD), a kind of aqueous pollutant (Akhgar and Pourghahramani 2015; Bryson and Crundwell 2014; Kantar et al. 2015; Ouyang et al. 2015; Pourghahramani and Akhgar 2015; Rozgonyi and Stirling 2015), and sulfur cycle in the earth's crust (Rickard and Luther 2007). Pyrite has also been considered as an ideal material for solar cells since 1980s. However, the low open-circuit voltage, which may result from gap state created by surface and bulk defects (Antonucci et al. 1991; Ennaoui et al. 1993) is the main barrier to the use of pyrite device. Therefore, the surface properties of pyrite are very important for all the mentioned aspects.

A large number of studies, including both experimental and theoretical ones, have been devoted to disclose the surface properties of pyrite. Low-energy electron diffraction (Pettenkofer et al. 1991), X-ray photoemission spectroscopy (Andersson et al. 2004; Leiro et al. 2003; Uhlig et al. 2001), ultraviolet photoelectron spectroscopy, (Pettenkofer et al. 1991), as well as scanning tunneling microscopy (Eggleston et al. 1996), were employed to characterize the (100) surface

✉ Jianxi Zhu
zhujx@gig.ac.cn

[1] CAS Key Laboratory of Mineralogy and Metallogeny/ Guangdong Provincial Key Laboratory of Mineral Physics and Materials, Guangzhou Institute of Geochemistry, Chinese Academy of Sciences (CAS), Guangzhou 510640, China

[2] CAS Center for Excellence in Deep Earth Science, Guangzhou 510640, China

[3] University of Chinese Academy of Sciences, Beijing 100049, China

structure of pyrite. These studies confirmed that the (100) surface is an unreconstructed surface. When S–S bonds are cleaved on (100) surface, the surface sulfur monomers (S^-) could convert into a more stable mono-sulfides (S^{2-}) through the reaction $Fe^{2+}_{surface} + S^-_{surface} \rightarrow Fe^{3+}_{surface} + S^{2-}_{surface}$ or $2S^-_{surface} \rightarrow S^{2-}_{surface} + S^0$ (Nesbitt et al. 1998). Results of both density functional theory (DFT) (Alfonso 2010; Hung et al. 2002a, b; Sun et al. 2011; Zhang et al. 2012) and classical force field (CFF) calculations (de Leeuw et al. 2000) were consistent with experiment, i.e., the (100) surface shows no significant relaxation.

Compared to pyrite (100) surface, knowledge about other naturally occurring pyrite surfaces is scanty even though (100), (210), (110), and (111) cleavages have been reported in literature (Mariano and Beger 1971). For the bulk terminated stoichiometric surfaces, (100), (210), (110) and (111) were studied by DFT calculations (Alfonso 2010; Hung et al. 2002a, b; Sun et al. 2011). Non-stoichiometric surfaces of all terminations were also considered with the first principles thermodynamic approach (Alfonso 2010). The comparison of the surface energies shows that the stability preference follows the order (100) > (111) > (210) > (110), which is inconsistent with the results from CFF calculations [(100) > (110) > (111)] (de Leeuw et al. 2000). All these first principles studies were performed by standard DFT calculations. Thus, the inconsistency may be caused from the coarse treating of the local electrons of 3*d* orbitals in the standard DFT framework (de Moreira et al. 2002). Therefore, a more accurate calculation method modifying the standard DFT approach is required. A promising way is to modify the intra-atomic Coulomb interaction through a DFT + *U* approach (Dudarev et al. 1998), which has been confirmed to be suitable for describing pyrite in DFT calculations (Zhang et al. 2012).

In this study, we investigate the structure, stability, and oxidation states of (100), (210), (110), and (111) surfaces of pyrite by using a DFT + *U* approach. Employing the thermodynamic approach, relative stabilities of considered surfaces in different sulfur environmental conditions were disclosed. With this correction, pyrite morphology distribution based on surface energy difference is consistent with those in natural and experimental systems. In addition, electron transfer between surface iron and sulfur atoms is also observed in this study.

Computational details

DFT calculations were performed using the plane-wave based Vienna Ab-initio Simulation Package (VASP) (Kresse and Furthmuller 1996). Generalized gradient approximation (GGA) formulation by Perdew, Burke, and Enzerhoff (PBE) (Perdew et al. 1996) was used to calculate the exchange–correlation term of the Kohn–Sham function. The projector-augmented wave (PAW) (Kresse and Joubert 1999) method was employed to describe the electron–ion interaction. Plane waves have been expanded to an energetic cutoff of 350 eV. The PBE form of the GGA exchange–correlation potentials have been used together with a simplified Hubbard *U* correction (GGA + *U*), introduced by Dudarev et al. (1998). In Dudarev's approach the parameters *U* and *J* do not enter separately, only the difference (*U*–*J*) is meaningful. A series of *U*–*J* were examined for the energy calculations of the pyrite surface. Considering both surface energy order and error minimization by Krishnamoorthy et al. (2013), the parameter *U*–*J* = 1.6 eV was employed to treat the Fe 3*d* orbitals for pyrite surfaces. The Bader charge-division scheme based on the electronic charge density (Bader 1985) was performed by the code developed by the Henkelman Group (Henkelman et al. 2006).

For integration within the Brillouin zone specific *k* points were selected using a 11 × 11 × 11 Monckhorst-Pack grid (Monkhorst and Pack 1976) for bulk pyrite unit cell. Similar to simulation models in Alfonso (2010), 17 terminations of pyrite (100), (210), (111), and (110) surfaces were constructed using slab models. 15 Å vacuum slabs are beneath the surfaces. Symmetrical surfaces were employed to avoid the artificial electric fields in the vacuum. All the Fe and S atoms were fully relaxed at their bulk positions during the structural optimization.

Cutting a surface from bulk pyrite along certain lattice plane (Fig. 1) will break bonds in pyrite, the density of broken bonds could be calculated as follows:

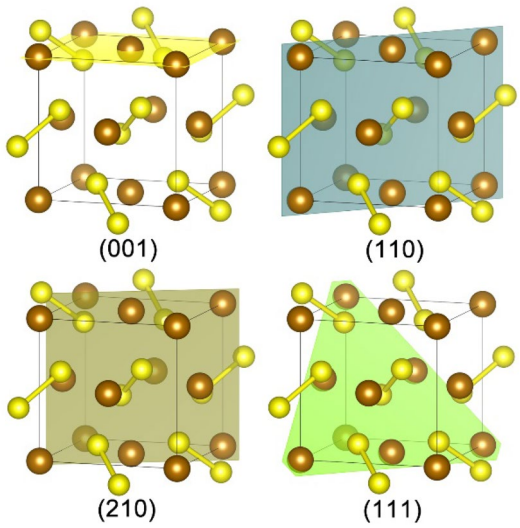

Fig. 1 Bulk unit cells of pyrite with (001), (110), (210), and (111) lattice planes. Brown spheres indicate Fe atoms and yellow spheres indicate S atoms

$$D_b = N_b/A, \quad (1)$$

where D_b and N_b are density and number of broken bonds on the surface, respectively, and A is the surface area. Details of all the surface models are presented in Table 1. For both (100) and (110) surfaces, Brillouin zone samplings were performed on a 6×6×1 Monkhorst–Pack grid (Monkhorst and Pack 1976); for (210) and (111) surfaces, the k-points meshes were set to 4×4×1 and 5×5×1, respectively. All the structures presented in this paper were rendered by VESTA freeware (Momma and Izumi 2008).

The surface energy, γ, at temperature T and pressure P is defined as

$$\gamma_{(T,P)} = \frac{1}{2A}\left[G^{surf} - N_{Fe}\mu_{Fe} - N_S\mu_S\right], \quad (2)$$

where G^{surf} is the Gibbs free energy of the slab, which can be approximately replaced by the total energy from DFT calculations (Reuter and Scheffler 2002); N_{Fe} and N_S are the numbers of Fe and S atoms in the slabs, respectively; μ_{Fe} and μ_S are the chemical potentials of Fe and S atoms, respectively; and they are correlated via $\mu_{Fe} + 2\mu_S = \mu_{FeS_2}$, where μ_{FeS_2} is the chemical potential of one FeS_2 formula in the bulk pyrite unit. To simulate different sulfur environments, $\Delta\mu_S$ is defined as the chemical potential difference of S between bulk pyrite (μ_S) and alpha phase bulk sulfur (E_S^{bulk}), which is considered as a S-rich environment ($\Delta\mu_S = 0$). Two preconditions, (i) FeS_2 does not decompose into Fe metal and sulfur and (ii) bulk sulfur does not condense on the surface, were proposed to estimate $\Delta\mu_S$ (Alfonso 2010), which could be expressed as

$$\Delta\mu_S = \mu_S - E_S^{bulk} < 0, \quad (3)$$

where $\Delta\mu_S < 0$ represents relatively S-lean environments.

Results and discussions

Bulk pyrite

The pyrite structure (Fig. 1) is a type of typical cubic configuration in both atmospheric-pressure (Rickard and Luther 2007) and high-pressure (Kuwayama et al. 2005) conditions with space group of $Pa3$. With parameter U–J = 1.6 eV (Krishnamoorthy et al. 2013), the calculated lattice constant of bulk pyrite from PBE + U is 5.423 Å and the indirect band gap is 0.95 eV (Fig. 2), which are in good agreement with the most widely accepted experimental data, 5.416 Å and 0.95 eV, respectively (Ferrer et al. 1990; Kleppe and Jephcoat 2004; Stevens et al. 1980). However, without U correction, the calculated band gap of bulk pyrite is just *ca*. 0.50 eV (much smaller than the experimental value), which is consistent with the findings of a previous DFT study (Zhang et al. 2012). The conventional DFT calculation gives relatively narrower band gaps for both semiconductor and insulator (de Moreira et al. 2002; Gross and Dreizler 2013). As U increases to 2 eV, the band gap increases

Table 1 Details for all the surface models used in this paper

No	Surface	S atom number	Fe atom number	S/Fe atomic ratio	Atomic layer number	Surface area (Å^2)	D_b (nm^{-2})
1	(100)-Fe	14	24	1.71	19	29.41	27.4
2	(100)-S*	14	28	2.00	21		13.6
3	(100)-2S	14	32	2.29	23		47.6
4	(110)-FeS	20	38	1.90	19	41.60	26.4
5	(110)-S*	18	36	2.00	19		19.2
6	(110)-2S	18	38	2.11	19		19.2
7	(111)-Fe	24	40	1.67	26	50.28	23.9
8	(111)-S	16	26	1.63	18		19.9
9	(111)-2S*	16	32	2.00	20		19.9
10	(111)-3S	16	38	2.38	22		23.9
11	(111)-4S	16	40	2.50	24		27.8
12	(210)-Fe	22	40	1.82	21	65.77	24.3
13	(210)-Fe′	18	32	1.78	17		18.2
14	(210)-S*	18	36	2.00	19		18.2
15	(210)-S′*	22	44	2.00	23		18.2
16	(210)-2S	18	40	2.22	19		24.3
17	(210)-2S′	18	40	2.22	19		18.2

*Denotes these surfaces are stoichiometric whereas the others are not

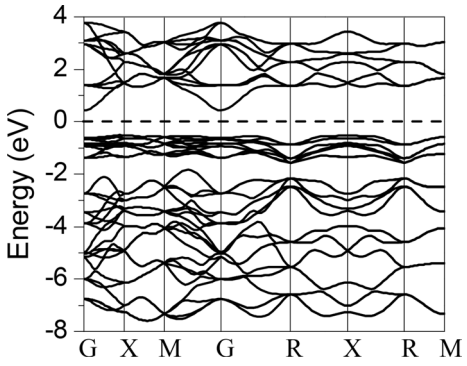

Fig. 2 PBE + *U* (*U* = 1.6 eV) band structure of bulk pyrite

to 1.02 eV (Hu et al. 2012; Zhang et al. 2012), which is a little lager than the actual value. On the other hand, when hybrid functions were employed, the band gap increases sharply to 2.66 eV (Krukau et al. 2006), may be due to the large amount of Hartree–Fork exchange (Labat et al. 2007). Therefore, appropriate Hubbard *U* correction is critical to describe pyrite correctly in DFT calculations. The band structure of bulk pyrite calculated from PBE + *U* is shown in Fig. 2. The conduction band (CB) edge is located at the Gamma point, which is consistent with previous DFT calculations, while a highly localized valance band (VB) with flat feature is obtained between − 0.5 and − 1.5 eV. Thus, we believe that the *U*–*J* = 1.6 eV is suitable for bulk pyrite.

Surface energies and determination of the Hubbard U value

Surface energies of pyrite are sensitive to the *U*–*J* parameter (Fig. 3). The calculated surface energies of pyrite under

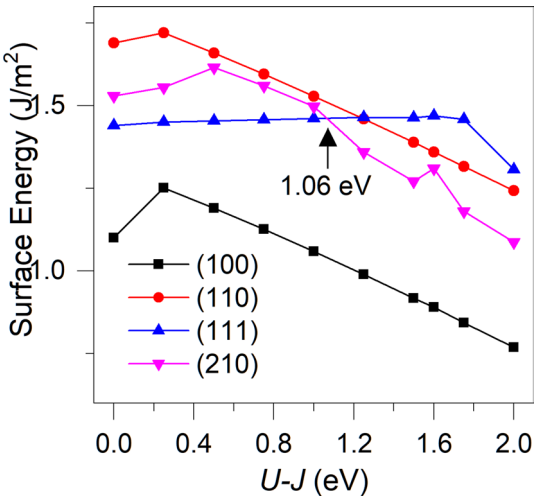

Fig. 3 Variation of surface energies of pyrite as a function of the *U*–*J* value

various *U*–*J* parameter show that the order of stoichiometric surface energies changes when the *U*–*J* parameter is introduced and greater than 1.06 eV. As the *U*–*J* > 1.06 eV, the order of stoichiometric surface energies changes to (100) < (210) < (110) < (111) (Table 2 and Fig. 3), different from that [(100) < (111) < (210) < (110)] in previous standard DFT studies (Alfonso 2010; Hung et al. 2002a, b; Sun et al. 2011; Zhang et al. 2012). Whether Hubbard *U* is introduced or not, the (100) surface, the most frequently observed surface in nature, has the lowest surface energy. The surface energies from previous DFT calculations are greater than those from the GGA(PBE) + *U* method. The small difference between energies of (100) surface derived by PBE + *U* may be due to different *U*–*J* parameters.

Forming a surface from bulk materials involves the breakage of bonds. The bond energy of Fe–S bonds in bulk pyrite is greater than 300 kJ/mol while that of S–S bonds is 245 kJ/mol (Nesbitt et al. 1998). Therefore, both S–S and Fe–S bonds are likely to be broken when a surface is cleaved from bulk pyrite. The density of broken bonds (DOB) on a certain surface is directly related to surface energy. Gao et al. (2014) employed surface energies of pyrite from DFT calculations without Hubbard *U* correction to examine the relationship between surface energy and DOB. However, only (100), (210) and (110) surfaces were considered. Energies of all the surfaces [(100), (111), (210), and (110)] are examined with the PBE + *U* method in the present study (Fig. 3). When the *U*–*J* value is smaller than 1.06 eV, the order of the surface energies disagrees with the DOBs of different surfaces. When the *U*–*J* value is greater than 1.06 eV, the surface energies order is consistent with the DOBs of different surfaces. Especially when *U*–*J* = 1.6 eV, a perfect linear relationship (with a R^2 greater than 0.99) between surface energy and DOB is built, as shown in Fig. 4a. An analysis of *R*-squared as a function of the *U*–*J* value from the linear fitting of the surface energy and DOBs (Fig. 4b) further confirms that the *U*–*J* = 1.6 eV is an optimal value to describe pyrite surfaces.

Table 2 Relaxed surface energies (J/m^2) of pyrite FeS_2; PBE + *U* results are compared with precious results

Surface	(100)	(210)	(111)	(110)
PBE (Hung et al. 2002a, b)	1.06	1.50	1.40	1.68
PBE (Sun et al. 2011)	1.04	1.49	1.43	1.72
PBE (Alfonso 2010)	1.21	1.61	1.49	1.79
LDA (Sun et al. 2011)	1.58	2.31	2.01	2.38
GGA + *U* (Zhang et al. 2012)	0.81	–	–	–
Classical force field (de Leeuw et al. 2000)	1.23		3.92	2.36
PBE (this study)	1.10	1.53	1.44	1.69
PBE + *U* (this study)	0.89	1.31	1.47	1.36

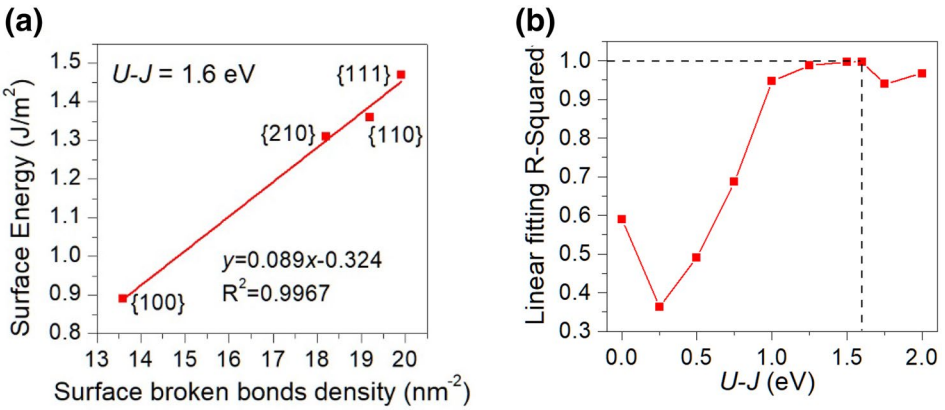

Fig. 4 **a** Linear relationship between surface energy and surface broken bonds density with a parameter of U–J = 1.6 eV; **b** variation of the linear fitting R-squared from the linear fitting of the surface energy and surface broken bonds density as a function of the U–J parameter

Theoretically, The Hubbard U value should be determined by using self-consistent calculations (Himmetoglu et al. 2014). The U value may vary site-by-site in different surface models (Huang et al. 2016), which may lead to a complicated understanding of the surface properties. The simple universal empirical U–J value of 1.6 eV observed in this study produces results that agree well with natural and experimental observations. Thus, we use the parameter of U–J = 1.6 eV for further calculations of surface structures and stabilities of pyrite.

Surface stabilities in different sulfur environment

As for the afore mentioned stoichiometric surfaces, surface energies are independent on μ_S. However, surface energies of nonstoichiometric surfaces are linear functions of μ_S. Variations of surface energies with chemical potential of S are displayed in Fig. 5. Not all the 17 considered surfaces are thermodynamically stable ones. The surfaces with excess Fe atoms are more stable under S lean conditions, which is consist with previous standard DFT calculation (Alfonso 2010).

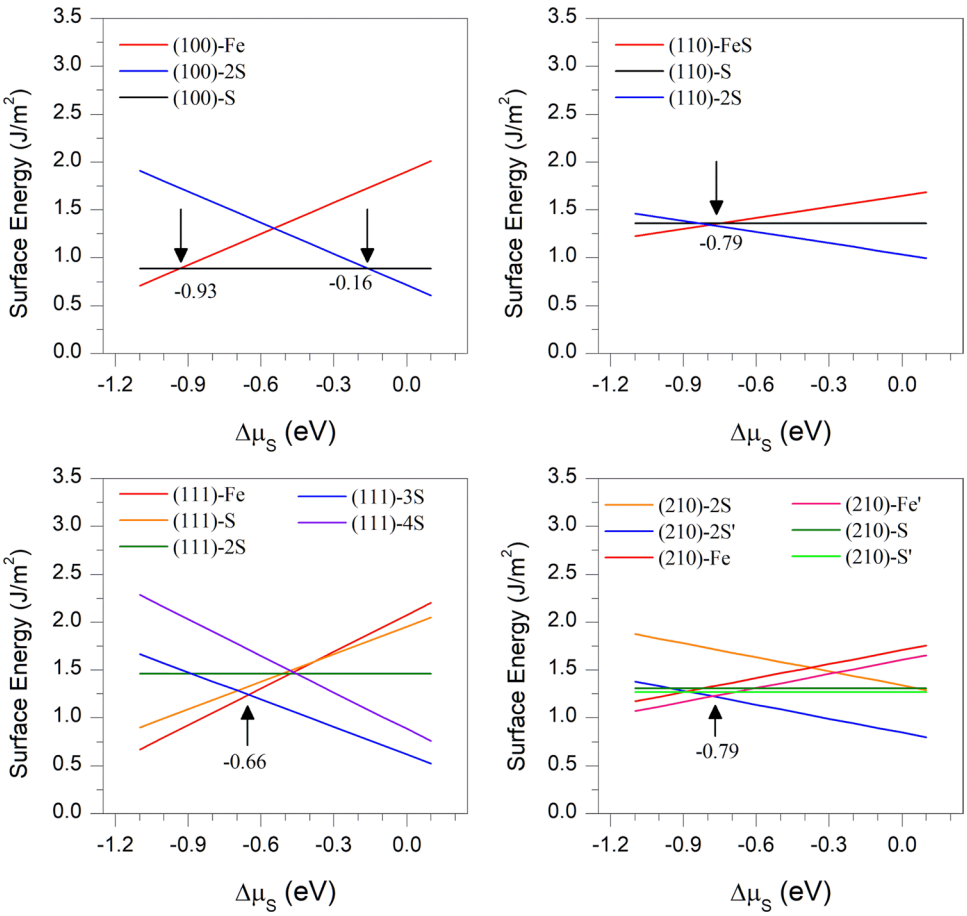

Fig. 5 Calculated surface energies (from PBE + U) of 17 possible pyrite surfaces as functions of sulfur chemical potential, $\Delta\mu_S$. $\Delta\mu_S = 0$ corresponds to the chemical potential of S atom in alpha phase bulk sulfur, which is considered as a relatively S-rich environment

All the thermodynamically stable surfaces could be true only in a certain range of S chemical potential. For (100) surfaces, the stable μ_S ranges of (100)-Fe, (100)-S, and (100)-2S are < -0.93 eV, [-0.93 eV, -0.16 eV], and > -0.16 eV, respectively. For the (110) surfaces, (110)-FeS and (110)-2S are stable at $\Delta\mu_S < -0.79$ eV and $\Delta\mu_S > -0.79$ eV, respectively, while (110)-S could not be thermodynamically stable in the whole $\Delta\mu_S$ range. For the (111) surfaces, only (111)-Fe and (111)-3S could be stable in a range of $\Delta\mu_S$ less and greater than -0.66 eV, respectively, whereas the other (111) surfaces are thermodynamically unstable. For the (210) surfaces, only (210)-Fe′ and (210)-2S′ are stable and they are interchanged at $\Delta\mu_S = -0.79$ eV. Thus, only 9 surfaces are thermodynamically stable, i.e., the (100)-Fe, (100)-S, (100)-2S, (110)-FeS, (110)-2S; (111)-Fe, (111)-3S, (210)-Fe′, and (210)-2S′ surfaces. Among these surfaces, only (100)-S is a stoichiometric surface while the others are nonstoichiometric. Among these surfaces, (111)-Fe was considered as a structural instable surface in previous DFT study without Hubbard U correction, which is not consistent with our results and could be attributed to the Hubbard U correction. These results are a little different to previous knowledge about the surface energies of pyrite, which only involves the stoichiometric surfaces, i.e., the (100)-S, (110)-S, (210)-S, and (111)-2S surfaces.

Energies of the nine thermodynamically stable pyritic surfaces are compared in Fig. 6. Between the two considered limits, S-lean and S-rich conditions, only two surfaces, (100)-S and (111)-3S, are the most stable ones. However, three surfaces were found to be the most energetically favorable ones in previous standard DFT study (Alfonso 2010), which may be due to the absence of the Hubbard U correction. At higher $\Delta\mu_S$, the (111)-3S is the most thermodynamically stable structure. For $\Delta\mu_S$ less than -0.29 eV, the (100)-S structure is the most energetically favorable.

The Wulff shape, i.e., the equilibrium shape of a single crystal (Herring 1951), of pyrite at different $\Delta\mu_S$ is shown in Fig. 7. The models were constructed from the surface energies in Fig. 6. At the S-lean limit (i.e., $\Delta\mu_S = -0.8$ eV), the Wulff shape is a truncated cube, {100} and {111} appear as the dominating facets. {111} facets degrade as $\Delta\mu_S$ increases. Further increase of $\Delta\mu_S$ leads to the appearance and grow of {210} facets. Then both {100} and {210} facets degrade as $\Delta\mu_S$ increases, and the Wulff shape becomes a truncated octahedron at the S-rich limit. Therefore, it can be concluded that the equilibrium shape of pyrite single crystal could change from truncated cube to truncated octahedron with the variation of sulfur environments. Although the {111} facet appears at both S-lean and S-rich limits, surface structures are different depending on the sulfur environments. At S-lean environment, it is an Fe excess surface, i.e., (111)-Fe. At S-rich environment, it is an S excess surface, i.e., (111)-3S. The same deduction could also be applied to {100} and {210} facets. As structures restrict the reactivity, the reactivity should be different for a certain facet formed in different sulfur environments.

According to analysis of the Wulff shape, only {100}, {210}, and {111} facets could appear on the equilibrium shapes in decreasing order, which consists with the morphology distribution in nature and synthetic systems. Chen et al. (1987) investigated the morphologies of 2495 pyrite crystals from four gold mines in three counties of the Jiaodong region in eastern Shandong province, China. The results indicate that {100}, {210}, and {111} are the most common single forms, the frequencies of appearance of which are arranged in decreasing order as 224:42.8:1. This order is identical to the order of surface energies observed in this

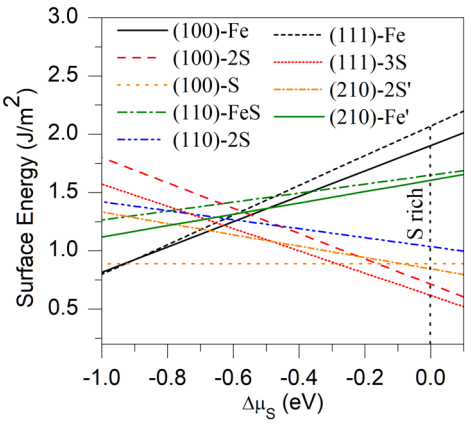

Fig. 6 Calculated surface free energies (from PBE + U) of nine relatively stable pyrite surfaces as functions of sulfur chemical potential, $\Delta\mu_S$. $\Delta\mu_S$= 0 corresponds to the chemical potential of S atom in alpha phase bulk sulfur, which is considered as a relatively S rich environment

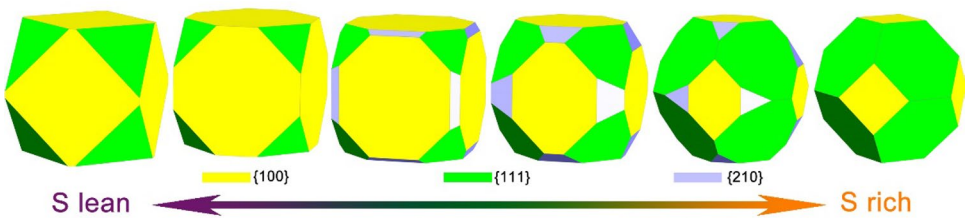

Fig. 7 Theoretical Wulff shape evolution of pyrite within the PBE + U under different sulfur environment (rendered by WinXMorph (Kaminsky 2007)). The S-rich shape corresponds to $\Delta\mu_S$ =0 while the S-lean one to $\Delta\mu_S$ = − 0.8 eV

study (Table 2). Chen et al. (1987) also concluded that {100} appears in general under low fugacity of sulfur (f_s) while {210} and {111} appear in general under high f_s. Hydrothermal experiments performed by Cai and Zhou (1994) reveal similar conclusions, i.e., pyritohedron {210} forms at high f_s, while pyrite cube {100} forms at relatively low f_s. These phenomena from natural and synthetic systems consist with our prediction of the Wulff shape from the PBE + U surface energy calculations in this study. The rigor of the PBE + U method is confirmed once again.

Relaxed surface structure and oxidation states

As (100)-Fe, (100)-S, (100)-2S, (111)-Fe, (111)-3S, (210)-Fe′, and (210)-2S′ surfaces can be thermodynamically stable, their relaxed structures were studied (Figs. 8, 9, 10). The structural optimizations (Table 3) show that: (i) (100)-Fe and (100)-2S surfaces reconstruct, surface Fe and S atoms of (100)-Fe become nearly on the same plane, and surface mono S atoms of (100)-2S rearrange to form S–S bonds; (ii) (111)-Fe and (111)-3S show no relaxations, and all the displacements of surface atoms are less than 0.05 Å; (iii) Surface atoms of (100)-S, (210)-Fe′, and (210)-2S′ show relaxation to a certain degree. Similar reconstructions of (100)-Fe and (100)-2S are also obtained in the previous GGA + U calculation (Zhang et al. 2012), which lead to coordination change of surface atoms as shown in Table 3. The bond length of the new formed S–S bond is 2.05 Å, which is shorter than that of the bulk S–S bond (2.16 Å), indicating that the new formed S–S bonds are stronger than those in bulk pyrite. No relaxations could be obtained on either (111)-Fe and (111)-3S, probably due to the nature of their relatively high surface energies, which may lead to higher surface reactivity. It is confirmed by previous surface oxidation experiments (Elsetinow et al. 2000; Guevremont et al. 1998; Xian et al. 2019; Zhu et al. 2018).

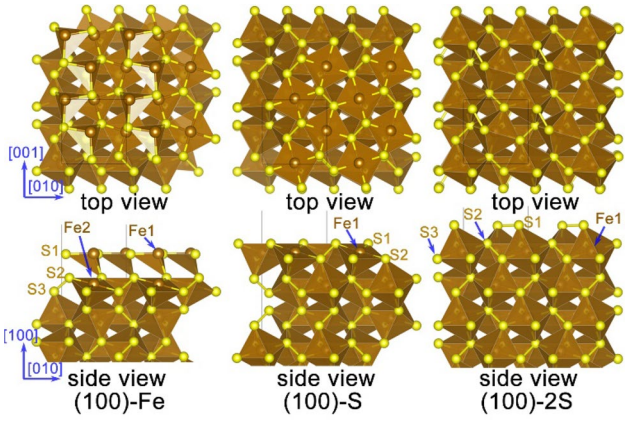

Fig. 8 Top and side views of the relaxed pyrite (100) surface configurations. Brown spheres indicate Fe atoms while yellow spheres indicate S atoms

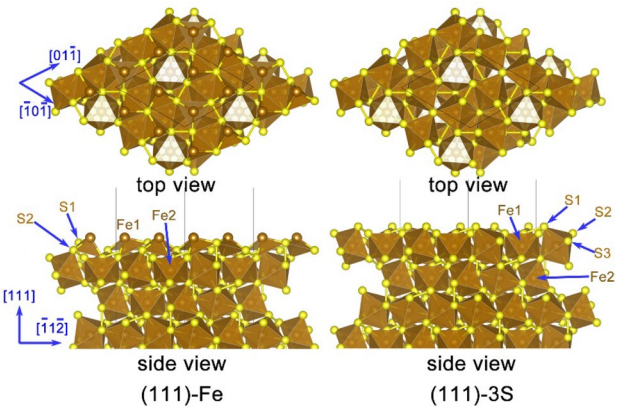

Fig. 9 Top and side views of the relaxed relative stable pyrite (111) surface configurations. Brown spheres indicate Fe atoms while yellow spheres indicate S atoms

The net charge of each atom of the relaxed surfaces was calculated using the Bader charge-division scheme (Table 3) (Bader 1985). The Bader charge of bulk Fe and S are + 0.61 e and − 0.30 e, respectively. To make the oxidation state (OS) naturally (Webster et al. 2016), the OS is assumed equal to 0.3 e in Bader charge. So, the OS for bulk Fe and S are + 2 and − 1, respectively. OSs of Fe and S in surfaces were approximatively calculated from the equation: OS = Bader charge/0.3, and the results were rounded-off to integer and presented in Table 3. All the OS results correspond to the natural oxidation state of Fe and S atoms except for S1 in (100)-Fe, whose OS is − 3, because the S atom gains more electrons.

Based on the OS analysis of Bader charges, we obtained the following: (i) for (100)-Fe, (100)-S, (210)-Fe′, and (210)-2S′ surfaces, electrons transfer from surface Fe to surface S atoms; (ii) (100)-2S, (111)-Fe, and (111)-3S surfaces show no significant charge transfer. The surface charge transfer could be described as

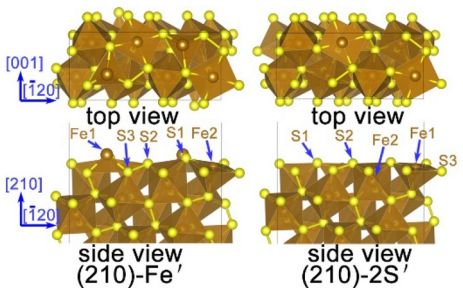

Fig. 10 Top and side views of the relaxed relative stable pyrite (210) surface configurations. Brown spheres indicate Fe atoms while yellow spheres indicate S atoms

Table 3 Relative stable pyrite surface atomic coordination, displacements and oxidation state

Surface	Atom label	Coordination	Δ*x* (Å)	Δ*y* (Å)	Δ*z* (Å)	Bader charge	Oxidation state[1]
(100)-Fe	Fe1*	3	0.26	−0.02	−0.13	0.95	+3
	Fe2	5	−0.03	−0.01	0.00	0.64	+2
	S1*	2	0.45	−0.27	0.44	−0.90	−3‡
	S2	4	0.00	0.03	−0.08	−0.35	−1
	S3	4	0.01	0.00	0.02	−0.34	−1
(100)-S	Fe1	5	0.06	0.09	0.04	0.76	+3
	S1*	3	−0.03	0.13	0.18	−0.36	−1
	S2*	4	0.01	0.12	0.16	−0.37	−1
(100)-2S	Fe1	6	−0.02	0.02	0.05	0.66	+2
	S1*	2	0.13	−0.16	0.06	−0.18	−1
	S2	3	−0.04	−0.09	0.02	−0.24	−1
	S3	4	0.07	−0.04	0.06	−0.34	−1
(111)-Fe	Fe1	3	0.00	0.00	0.00	0.53	+2
	Fe2	6	0.00	0.00	0.00	0.63	+2
	S1	4	0.00	0.00	0.00	−0.46	−1
	S2	4	0.00	0.00	0.00	−0.44	−1
(111)-3S	Fe1	6	0.01	0.02	0.02	0.73	+2
	Fe2	6	0.00	0.00	−0.01	0.63	+2
	S1	2	−0.01	−0.02	−0.04	−0.16	−1
	S2	3	0.03	0.05	0.03	−0.24	−1
	S3	3	0.00	0.00	0.00	−0.45	−1
(210)-Fe′	Fe1*	3	0.19	0.01	−0.13	0.87	+3
	Fe2	5	−0.01	−0.02	0.00	0.75	+2
	S1*	3	0.30	−0.03	0.44	−0.77	−2
	S2	3	−0.05	0.02	0.09	−0.36	−1
	S3	4	−0.06	0.10	0.00	−0.39	−1
(210)-2S′	Fe1*	5	−0.04	−0.03	−0.14	0.76	+3
	Fe2	6	−0.03	0.06	0.06	0.69	+2
	S1*	2	0.23	0.06	0.03	−0.46	−2
	S2	3	−0.04	−0.01	0.05	−0.30	−1
	S3	4	0.04	0.00	0.06	−0.29	−1

*Denotes these atoms on pyrite surfaces relaxed significantly, which is differentiated while the displacements are larger than 0.1 Å

[1]Oxidation states (OS) were approximatively calculated from the equation: OS = Bader charge/0.3, and the results were rounded-off to integer

‡This S atom gains more electrons than the other S atoms with OS of −2

$Fe^{2+}_{surface} + S^{-}_{surface} \rightarrow Fe^{3+}_{surface} + S^{2-}_{surface}$, which was confirmed by their X-ray photoemission spectra (Nesbitt et al. 1998). However, only four thermodynamically stable surfaces exhibit charge transfer while the others do not. Charge transfer on the (100)-2S surface is probably due to the forming of S–S bonds during the relaxation, which could make the structure more stable. Charge transfer does not occur on either (111)-Fe and (111)-3S, probably because of no relaxation exhibited on these surfaces, which is consistent with the relatively higher surface energy and lower appearance frequency in nature (Chen et al. 1987).

Implications

Our results demonstrate that the Hubbard *U* correction is not only an important issue in solving electronic problems, but also a critical improvement for evaluating the surface structure and chemical composition, as well as stability, of pyrite. Therefore, we suggest that the local 3*d* or 4*f* orbital correction within the standard DFT framework must be considered when dealing with scientific problems of the surfaces of minerals containing *d* or *f* electrons. The surface energy sequence predicted in this study may represent

the true sequence of pyrite surface energies in the natural world. Knowledge of the sequence of pyrite surface energies could be used as guidance for controlled syntheses of pyrite materials with specific surface chemical composition and/or atomic configuration. Furthermore, the crystal shape and chemistry can be employed as an indicator for its formation conditions (Xing et al. 2019). The sulfur chemical potential dependent surface energies (i.e., the equilibrium shape) is fundamental in interpreting pyrite formation in various sulfur conditions. The ambient sulfur condition dependent atomic configurations and oxidation states of surface atoms could also be utilized as surface typostructure and typochemistry.

Conclusions

In summary, we used PBE + U to elucidate the surface structure and stability of pyrite in different sulfur environments. We find that the U correction is a critical parameter in DFT calculations to describe the structure and stability of pyrite surfaces. With the U correction, the surface energy order for stoichiometric surfaces is (100) < (210) < (110) < (111), which is different from previous knowledge from conventional DFT calculations, but consistent with morphology distribution in natural and synthetic systems in different sulfur conditions. Between S-lean and S-rich conditions, only two surfaces, (100)-S and (111)-3S, are the most stable surfaces. The equilibrium shape of pyrite single crystal could change from truncated cube to truncated octahedron with the variation of S environment. (100)-Fe, (100)-S, (100)-2S, (111)-Fe, (111)-3S, (210)-Fe′, and (210)-2S′ are relatively stable surfaces. (100)-Fe and (100)-2S reconstruct, and (111)-Fe and (111)-3S show no relaxations while (100)-S, (210)-Fe′, and (210)-2S′ show relaxation to certain degree. Charge transfer could be found on (100)-Fe, (100)-S, (210)-Fe′, and (210)-2S′ surfaces, which could be described as $Fe^{2+}_{surface} + S^{-}_{surface} \rightarrow Fe^{3+}_{surface} + S^{2-}_{surface}$, while no charge transfer occurs on other surfaces. The charge transfer may be the reason responsible for the stability of natural pyrite {100} and {210} facets. These findings not only emphasize the importance of Hubbard U correction for DFT calculation of pyrite surfaces, but also disclose the surface structure and stability of pyrite.

Acknowledgements The authors acknowledge two anonymous reviewers for their helpful comments and suggestions. This study was supported by the fund from the National Natural Science Foundation of China (Grant nos. 41825003 and 41921003), the Youth Innovation Promotion Association CAS (Grant no. 2021353), the Natural Science Foundation of Guangdong Province, China (Grant no. 2019A1515011303), Guangdong Special Support Program (Grant no. 2019TX05L169), the Tuguangchi Award for Excellent Young Scholar GIG, CAS, and the Science and Technology Planning of Guangdong Province, China (2017B030314175 & 2020B1212060055). This is a contribution No.IS-3001 from GIGCAS.

Declarations

Conflict of interest The authors declare no conflicts of interest or competing interests in any of the material discussed in this article.

References

Akhgar BN, Pourghahramani P (2015) Impact of mechanical activation and mechanochemical activation on natural pyrite dissolution. Hydrometallurgy 153:83–87. https://doi.org/10.1016/j.hydromet.2015.02.010

Alfonso DR (2010) Computational investigation of FeS2 surfaces and prediction of effects of sulfur environment on stabilities. J Phys Chem C 114:8971–8980. https://doi.org/10.1021/jp100578n

Andersson K et al (2004) Experimental and theoretical characterization of the structure of defects at the pyrite FeS2(100) surface. Phys Rev B 70:195404. https://doi.org/10.1103/PhysRevB.70.195404

Antonucci V, Arico AS, Giordano N, Antonucci PL, Russo U, Cocke DL, Crea F (1991) Photoactive screen-printed pyrite anodes for electrochemical photovoltaic cells. Sol Cells 31:119–141. https://doi.org/10.1016/0379-6787(91)90016-I

Bader RFW (1985) Atoms in molecules. Acc Chem Res 18:9–15. https://doi.org/10.1021/ar00109a003

Bryson LJ, Crundwell FK (2014) The anodic dissolution of pyrite (FeS2) in hydrochloric acid solutions. Hydrometallurgy 143:42–53. https://doi.org/10.1016/j.hydromet.2014.01.005

Cai Y-J, Zhou M (1994) Crystalomorphological characteristics of pyrite in hydrothermal gold deposit—an experimental study. Sci China (Ser B) 37:117–128

Chen G, Sun D, Zhang L, Zang W, Wang J, Lu A (1987) Morphogenesis of pyrite. Geoscience 1:60–76

Chen JH, Lan LH, Chen Y (2013) Computational simulation of adsorption and thermodynamic study of xanthate, dithiophosphate and dithiocarbamate on galena and pyrite surfaces. Miner Eng 46–47:136–143. https://doi.org/10.1016/j.mineng.2013.03.015

de Leeuw NH, Parker SC, Sithole HM, Ngoepe PE (2000) Modeling the surface structure and reactivity of pyrite: Introducing a potential model for FeS2. J Phys Chem B 104:7969–7976

de Moreira PRI, Illas F, Martin RL (2002) Effect of Fock exchange on the electronic structure and magnetic coupling in NiO. Phys Rev B 65:155102. https://doi.org/10.1103/PhysRevB.65.155102

Deng MJ, Karpuzov D, Liu QX, Xu ZH (2013) Cryo-XPS study of xanthate adsorption on pyrite. Surf Interface Anal 45:805–810. https://doi.org/10.1002/sia.5165

Dudarev SL, Botton GA, Savrasov SY, Humphreys CJ, Sutton AP (1998) Electron-energy-loss spectra and the structural stability of nickel oxide: an LSDA+U study. Phys Rev B 57:1505–1509. https://doi.org/10.1103/PhysRevB.57.1505

Eggleston CM, Ehrhardt JJ, Stumm W (1996) Surface structural controls on pyrite oxidation kinetics: an XPS-UPS, STM, and modeling study. Am Mineral 81:1036–1056. https://doi.org/10.2138/am-1996-9-1002

Elsetinow AR, Guevremont JM, Strongin DR, Schoonen MAA, Strongin M (2000) Oxidation of 100 and 111 surfaces of pyrite: effects of preparation method. Am Mineral 85:623–626. https://doi.org/10.2138/am-2000-0428

Ennaoui A et al (1993) Iron disulfide for solar-energy conversion. Sol Energ Mat Sol C 29:289–370. https://doi.org/10.1016/0927-0248(93)90095-K

Ferrer IJ, Nevskaia DM, Delasheras C, Sanchez C (1990) About the Band-Gap Nature of Fes2 as Determined from Optical and Photoelectrochemical Measurements Solid State Commun 74:913–916. https://doi.org/10.1016/0038-1098(90)90455-K

Gao ZY, Sun W, Hu YH (2014) Mineral cleavage nature and surface energy: anisotropic surface broken bonds consideration. T Nonferr Metal Soc 24:2930–2937. https://doi.org/10.1016/S1003-6326(14)63428-2

Gross EK, Dreizler RM (2013) Density functional theory, vol 337. Springer Science & Business Media, New York

Guevremont JM, Elsetinow AR, Strongin DR, Bebie J, Schoonen MAA (1998) Structure sensitivity of pyrite oxidation: Comparison of the (100) and (111) planes. Am Mineral 83:1353–1356. https://doi.org/10.2138/am-1998-11-1225

Henkelman G, Arnaldsson A, Jonsson H (2006) A fast and robust algorithm for Bader decomposition of charge density. Comp Mater Sci 36:354–360. https://doi.org/10.1016/j.commatsci.2005.04.010

Herring C (1951) Some theorems on the free energies of crystal surfaces. Phys Rev 82:87–93. https://doi.org/10.1103/PhysRev.82.87

Himmetoglu B, Floris A, de Gironcoli S, Cococcioni M (2014) Hubbard-corrected DFT energy functionals: The LDA+U description of correlated systems. Int J Quantum Chem 114:14–49. https://doi.org/10.1002/qua.24521

Hu J, Zhang Y, Law M, Wu R (2012) Increasing the band gap of iron pyrite by alloying with oxygen. J Am Chem Soc 134:13216–13219. https://doi.org/10.1021/ja3053464

Huang X, Ramadugu SK, Mason SE (2016) Surface-specific DFT + U approach applied to α-Fe2O3(0001). J Phys Chem C 120:4919–4930. https://doi.org/10.1021/acs.jpcc.5b12144

Hung A, Muscat J, Yarovsky I, Russo SP (2002a) Density-functional theory studies of pyrite FeS2 (111) and (210) surfaces. Surf Sci 520:111–119. https://doi.org/10.1016/S0039-6028(02)02294-X

Hung A, Muscat J, Yarovsky I, Russo SP (2002b) Density-functional theory studies of pyrite FeS2(100) and (110) surfaces. Surf Sci 513:511–524. https://doi.org/10.1016/S0039-6028(02)01849-6

Kaminsky W (2007) From CIF to virtual morphology using the WinXMorph program. J Appl Crystallogr 40:382–385. https://doi.org/10.1107/S0021889807003986

Kantar C, Ari C, Keskin S, Dogaroglu ZG, Karadeniz A, Alten A (2015) Cr(VI) removal from aqueous systems using pyrite as the reducing agent: batch, spectroscopic and column experiments. J Contam Hydrol 174:28–38. https://doi.org/10.1016/j.jconhyd.2015.01.001

Kleppe AK, Jephcoat AP (2004) High-pressure Raman spectroscopic studies of FeS2 pyrite. Mineral Mag 68:433–441. https://doi.org/10.1180/0026461046830196

Kresse G, Furthmuller J (1996) Efficiency of ab-initio total energy calculations for metals and semiconductors using a plane-wave basis set. Comp Mater Sci 6:15–50. https://doi.org/10.1016/0927-0256(96)00008-0

Kresse G, Joubert D (1999) From ultrasoft pseudopotentials to the projector augmented-wave method. Phys Rev B 59:1758–1775. https://doi.org/10.1103/PhysRevB.59.1758

Krishnamoorthy A, Herbert FW, Yip S, Van Vliet KJ, Yildiz B (2013) Electronic states of intrinsic surface and bulk vacancies in FeS2. J Phys Condens Matter 25:045004. https://doi.org/10.1088/0953-8984/25/4/045004

Krukau AV, Vydrov OA, Izmaylov AF, Scuseria GE (2006) Influence of the exchange screening parameter on the performance of screened hybrid functionals. J Chem Phys 125:224106. https://doi.org/10.1063/1.2404663

Kuwayama Y, Hirose K, Sata N, Ohishi Y (2005) The pyrite-type high-pressure form of silica Science 309:923–925. https://doi.org/10.1126/science.1114879

Labat F, Baranek P, Domain C, Minot C, Adamo C (2007) Density functional theory analysis of the structural and electronic properties of TiO2 rutile and anatase polytypes: performances of different exchange-correlation functionals. J Chem Phys 126:154703. https://doi.org/10.1063/1.2717168

Leiro JA, Mattila SS, Laajalehto K (2003) XPS study of the sulphur 2p spectra of pyrite. Surf Sci 547:157–161. https://doi.org/10.1016/j.susc.2003.09.033

Mariano AN, Beger RM (1971) Cleavage in Pyrite and Cobaltite. Am Mineral 56:1867–2000

Momma K, Izumi F (2008) VESTA: a three-dimensional visualization system for electronic and structural analysis. J Appl Crystallogr 41:653–658. https://doi.org/10.1107/S0021889808012016

Monkhorst HJ, Pack JD (1976) Special points for Brillouin-Zone integrations. Phys Rev B 13:5188–5192. https://doi.org/10.1103/PhysRevB.13.5188

Murphy R, Strongin DR (2009) Surface reactivity of pyrite and related sulfides. Surf Sci Rep 64:1–45. https://doi.org/10.1016/j.surfrep.2008.09.002

Nesbitt HW, Bancroft GM, Pratt AR, Scaini MJ (1998) Sulfur and iron surface states on fractured pyrite surfaces. Am Mineral 83:1067–1076. https://doi.org/10.2138/am-1998-9-1015

Ouyang YT, Liu Y, Zhu RL, Ge F, Xu TY, Luo Z, Liang LB (2015) Pyrite oxidation inhibition by organosilane coatings for acid mine drainage control. Miner Eng 72:57–64. https://doi.org/10.1016/j.mineng.2014.12.020

Perdew JP, Burke K, Ernzerhof M (1996) Generalized gradient approximation made simple. Phys Rev Lett 77:3865–3868. https://doi.org/10.1103/PhysRevLett.77.3865

Pettenkofer C, Jaegermann W, Bronold M (1991) Site specific surface interaction of electron-donors and acceptors on Fes 2(100) cleavage Planes Ber Bunsen. Phys Chem 95:560–565. https://doi.org/10.1002/bbpc.19910950504

Pourghahramani P, Akhgar BN (2015) Influence of mechanical activation on the reactivity of natural pyrite in lead (II) removal from aqueous solutions. J Ind Eng Chem 25:131–137. https://doi.org/10.1016/j.jiec.2014.10.023

Reuter K, Scheffler M (2002) Composition, structure, and stability of RuO2(110) as a function of oxygen pressure. Phys Rev B. https://doi.org/10.1103/PhysRevB.65.035406

Rickard D, Luther GW (2007) Chemistry of iron sulfides. Chem Rev 107:514–562. https://doi.org/10.1021/cr0503658

Rozgonyi T, Stirling A (2015) DFT study of oxidation states on pyrite surface sites. J Phys Chem C 119:7704–7710. https://doi.org/10.1021/acs.jpcc.5b01943

Stevens ED, Delucia ML, Coppens P (1980) Experimental-observation of the effect of crystal-field splitting on the electron-density distribution of iron pyrite. Inorg Chem 19:813–820. https://doi.org/10.1021/ic50206a006

Sun RS, Chan MKY, Ceder G (2011) First-principles electronic structure and relative stability of pyrite and marcasite: implications for photovoltaic performance. Phys Rev B. https://doi.org/10.1103/PhysRevB.83.235311

Uhlig I, Szargan R, Nesbitt HW, Laajalehto K (2001) Surface states and reactivity of pyrite and marcasite. Appl Surf Sci 179:222–229. https://doi.org/10.1016/S0169-4332(01)00283-5

Webster AJ, Mueller CM, Foegen NP, Sit PHL, Speetzen ED, Cunningham DW, D'Acchioli JS (2016) Oxidation states "naturally": a natural bond orbital method for determining transition metal oxidation states. Polyhedron 114:128–132. https://doi.org/10.1016/j.poly.2015.11.018

Xian HY et al (2019) Crystal habit-directed gold deposition on pyrite: Surface chemical interpretation of the pyrite morphology indicative of gold enrichment. Geochim Cosmochim Ac 264:191–204. https://doi.org/10.1016/j.gca.2019.08.011

Xing Y, Brugger J, Tomkins A, Shvarov Y (2019) Arsenic evolution as a tool for understanding formation of pyritic gold ores. Geology 47:335–338. https://doi.org/10.1130/G45708.1

Yang B, Tong X, Deng ZB, Lv XW (2016) The adsorption of Cu species onto pyrite surface and its effect on pyrite flotation. J Chem-Ny. https://doi.org/10.1155/2016/4627929

Zhang YN, Hu J, Law M, Wu RQ (2012) Effect of surface stoichiometry on the band gap of the pyrite FeS2(100) surface. Phys Rev B 85:085314. https://doi.org/10.1103/PhysRevB.85.085314

Zhang YH, Cao Z, Cao YD, Sun CY (2013) FTIR studies of xanthate adsorption on chalcopyrite, pentlandite and pyrite surfaces. J Mol Struct 1048:434–440. https://doi.org/10.1016/j.molstruc.2013.06.015

Zhu J et al (2018) Surface structure-dependent pyrite oxidation in relatively dry and moist air: implications for the reaction mechanism and sulfur evolution. Geochim Cosmochim Ac 228:259–274. https://doi.org/10.1016/j.gca.2018.02.050